

RevBiFPN: The Fully Reversible Bidirectional Feature Pyramid Network

Vitaliy Chiley¹ Vithursan Thangarasa¹ Abhay Gupta¹ Anshul Samar¹ Joel Hestness¹ Dennis DeCoste¹

Abstract

This work introduces the RevSilo, the first reversible module for bidirectional multi-scale feature fusion. Like other reversible methods, RevSilo eliminates the need to store hidden activations by recomputing them. Existing reversible methods, however, do not apply to multi-scale feature fusion and are therefore not applicable to a large class of networks. Bidirectional multi-scale feature fusion promotes local and global coherence and has become a de facto design principle for networks targeting spatially sensitive tasks e.g. HRNet (Sun et al., 2019a) and EfficientDet (Tan et al., 2020). When paired with high-resolution inputs, these networks achieve state-of-the-art results across various computer vision tasks, but training them requires substantial accelerator memory for saving large, multi-resolution activations. These memory requirements cap network size and limit progress. Using reversible recomputation, the RevSilo alleviates memory issues while still operating across resolution scales. Stacking RevSilos, we create RevBiFPN, a fully reversible bidirectional feature pyramid network. For classification, RevBiFPN is competitive with networks such as EfficientNet while using up to 19.8x lesser training memory. When fine-tuned on COCO, RevBiFPN provides up to a 2.5% boost in AP over HRNet using fewer MACs and a 2.4x reduction in training-time memory.

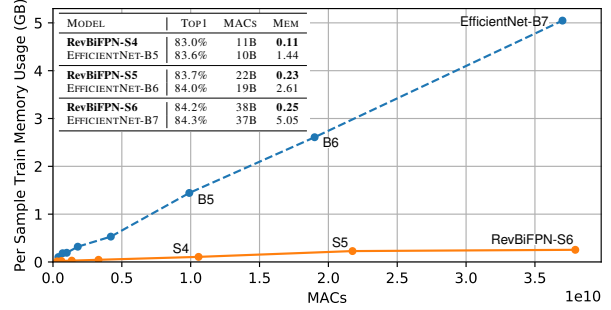


Figure 1. MACs vs Measured Memory Usage for ImageNet Training on 1 GPU: RevBiFPNs significantly outperform EfficientNets at all scales. In particular, RevBiFPN-S6 achieves comparable accuracy (84.2%) to EfficientNet-B7 on ImageNet while using comparable MACs (38.1B) and 19.8x lesser training memory per sample. Details in Table 2 and Table 11 (in Appendix F).

Even when resources are optimally allocated, scaling networks produces large feature maps thus training requires large amount of accelerator memory (Figure 1). While low-resolution intermediate representations work well for classification tasks (LeCun et al., 1998; Krizhevsky et al., 2012; Simonyan & Zisserman, 2015; Tan & Le, 2019), dense prediction tasks, such as detection and segmentation, require the construction of spatially informative, high-resolution feature maps which further exacerbates memory issues.

U-Net (Ronneberger et al., 2015), used for segmentation, was one of the first multi-scale feature fusion networks. Initially, detection networks would perform multi-scale inference by processing every scale of an image pyramid independently, but they soon adopted multi-scale feature fusion to directly produce a feature pyramid, i.e. multi-scale features (Lin et al., 2017a;b; Redmon & Farhadi, 2018). Bidirectional multi-scale feature fusion networks iteratively merge information between high and low resolution feature maps, producing robust (Hendrycks & Dietterich, 2019) scale invariant models. These models promote local and global coherence by iteratively aligning the semantic representations of fine-grained and high-level features. As a result, these networks are often the backbone of SOTA computer vision systems (Liu et al., 2018; Cai & Vasconcelos, 2018; Sun et al., 2019a; Tan et al., 2020), but the memory requirements of backpropagating through multi-scale feature fusion complicate training and limit scalability. Training

1. Introduction

State-of-the-art (SOTA) computer vision (CV) networks have large memory requirements that complicate training and limit scalability. Tan & Le (2019) and Dollár et al. (2021) show how compound scaling, i.e. scaling input resolution, network width, and depth, results in efficient networks across a wide range of parameter and MAC counts.

¹Cerebras Systems, Sunnyvale, CA, USA. Correspondence to: Vitaliy Chiley <vitaliy@cerebras.net>.

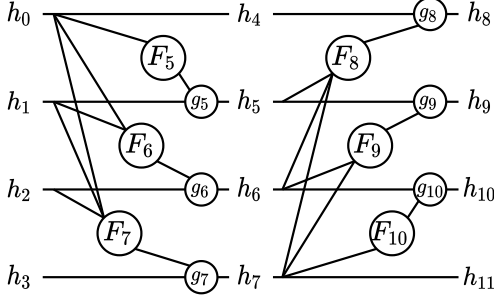


Figure 2. An $N = 4$ RevSilo. The left half generalizes the affine coupling block of Dinh et al. (2014).

CV networks pushes the memory bounds of modern hardware with hardware memory setting a hard limit on how far researchers scale these networks, enforcing an upper bound on network performance.

Hidden activations are needed to compute the gradient of the loss with respect to a neural network’s parameters. Traditionally, the activations computed during the forward pass are cached for use in the backward pass. While this method of neural network training has worked well in the past, the growth of neural networks has outpaced increases in accelerator memory. Motivated by flow structures (Dinh et al., 2017; Kingma & Dhariwal, 2018), Gomez et al. (2017) recognized that if a network is designed using a series of invertible operations the activations can be recomputed during the backward pass. Using this paradigm, reversible networks perform “backpropagation without storing activations” (Gomez et al., 2017), reducing their activation memory complexity with respect to depth from linear to constant. Although reversible structures have been successfully used in image classification (Gomez et al., 2017; Jacobsen et al., 2018) and language modeling (Kitaev et al., 2020; MacKay et al., 2018), they have yet to be used where they are needed most: in multi-scale feature fusion networks to produce high-resolution feature maps. Appendix A provides further context for this work.

1.1. Contributions

To address the memory challenges of training models for spatially sensitive tasks, this work introduces the RevSilo and the network built with it, RevBiFPN. The main contributions of this work are:

1. The RevSilo (Figure 2), the first bidirectional multi-scale feature fusion module that is invertible.
2. RevBiFPN (Figure 3) is the first fully reversible bidirectional multi-scale feature fusion pyramid network. It is built using the RevSilo and uses a fraction of the memory when compared to the same network without reversible recomputation (Figures 1, 4 to 6 and 12).
3. With a classification head, RevBiFPN is pretrained on

ImageNet (Deng et al., 2009) to accuracies competitive with networks designed specifically for classification (Figure 1 and Section 4.1).

4. To our knowledge, this work is the first to fine-tune a reversible backbone on downstream CV tasks. With the appropriate heads, RevBiFPN is competitive with similar networks on detection and segmentation tasks while using a fraction of the accelerator memory for training (Section 4.2).

2. Reversible Residual Silo

The Reversible Residual Silo, or RevSilo, generalizes both affine coupling (Dinh et al., 2014) and the reversible residual block (Gomez et al., 2017) to create an invertible module for bidirectional multi-scale feature fusion. Figure 2 shows two halves of the RevSilo with $N = 4$ spatial resolutions. The left half communicates information down the feature pyramid and the right sends information up the feature pyramid. g_i can be any, potentially parameterized, invertible transformation. In this work, g_i is element-wise addition, and therefore its inverse, g_i^{-1} , is element-wise subtraction for all i . If h_i and h_j are on the same row, i.e. $i \% N == j \% N$, the RevSilo’s residual structure requires that the shape of h_i equals the shape of h_j . Otherwise, F_i should transform the shape of its inputs to match the shape of h_i . Besides this shape constraint, F_i can be any transformation. The RevSilo construct remain invertible even if some inputs are set to 0. Setting h_3 to 0 can, for example, be used to expand an $N = 3$ feature pyramid into an $N = 4$ feature pyramid. Appendix B shows the equations for the $N = 4$ RevSilo depicted in Figure 2.

3. RevBiFPN

RevBiFPN uses the RevSilo to create a fully reversible backbone that utilizes bidirectional multi-scale feature fusion and produces a feature pyramid output. Directly using a reversible multi-scale feature fusion module, RevBiFPN circumvents the issues seen in the RevNet and i-RevNet design (Appendix A). The high-level network structure of RevBiFPN is shown in Figure 3. The output feature pyramid can then be used as an input to different task-specific heads (Appendix C.5).

The network uses the invertible SpaceToDepth stem (Ridnik et al., 2021; Shi et al., 2016; Dinh et al., 2017; Jacobsen et al., 2018) to initially downsample the input by a factor of 4 and produce $c = 4^2 \times 3 = 48$ channels. The baseline model (RevBiFPN-S0) uses $c_0 = 48$, $c_1 = 64$, $c_2 = 80$, and $c_3 = 160$ channels in its $N = 4$ spatial resolutions. As the network size is increased, the input image channels are duplicated to ensure the network is fully reversible regardless of network width. The rest of the network has a structure similar to HRNet (Sun et al., 2019a) where transfor-

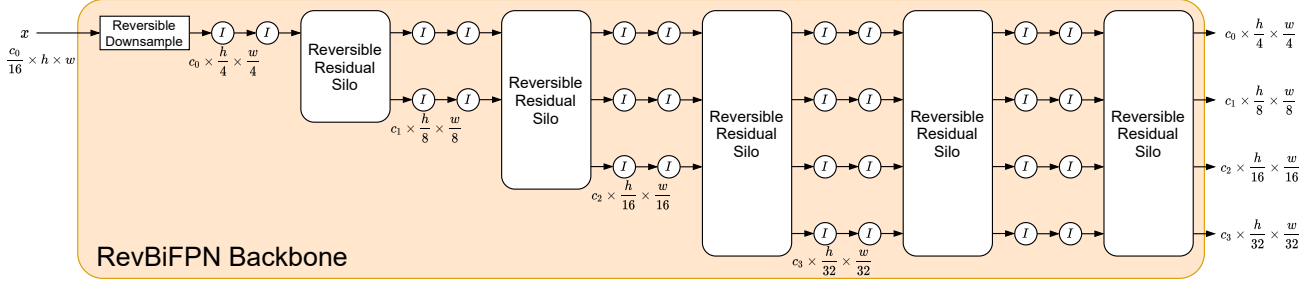


Figure 3. A RevBiFPN that creates an $N = 4$ feature pyramid. Given the output feature pyramid, all activations can be recomputed going backwards through the network. The I components are reversible residual blocks. The network builds an $N = 4$ multi-scale hidden representation using 3 RevSilos and has an extra depth of $d = 2$ RevSilos for further feature fusion.

mations in the same spatial resolution use reversible residual blocks (Gomez et al., 2017).

For simplicity, the network uses the RevSilo variant shown in Figure 11 (in Appendix B.1). Here, the F operations independently transform each input and sum them together. The network isn’t designed with a specific hardware target in mind and therefore uses the MBConv Block (Howard et al., 2017), a building block that efficiently utilizes parameters and multiply-accumulates (MAC).² The MBConv Block is used for both transformations in the reversible residual blocks and also the F transformations of the RevSilo. Using the MBConv Block in network design produces networks that have fast on inference devices (Howard et al., 2017; Sandler et al., 2018; Howard et al., 2019; Tan & Le, 2019; Mehta & Rastegari, 2021).

Within its RevSilos, RevBiFPN upsamples and downsamples features by factors of 2. To upsample a feature by a factor of 2^k , the depthwise convolution of the MBConv Block uses a stride of 1 and a kernel size of 3 or 5; this is then followed by bilinear upsampling. To downsample a feature by a factor of 2^k , the depthwise convolution of the MBConv Block uses a stride of 2^k and a kernel size of $2^{k+1} \pm 1$. As a result, the network uses a diverse set of kernel sizes as suggested by Tan et al. (2019). Network parameters are initialized using Kaiming initialization (He et al., 2015). Batch Normalization biases are initialized to zero and weights are initialized to one, except the weights of the normalization layer before a residual add which are initialized to zero to promote stability (Kingma & Dhariwal, 2018).

The network uses the MBConv variant with squeeze-excite layers (Tan & Le, 2019) and the hard-swish non-linearity (Howard et al., 2019). The network has larger expansion ratios on the lower resolution streams and uses larger squeeze-excite ratios on the large resolution streams (Ridnik et al., 2021). With a classification head, the result-

²ML researchers often use FLOP when they mean MAC. This work uses MAC to mean multiply-accumulate since FLOP means a single floating point operation.

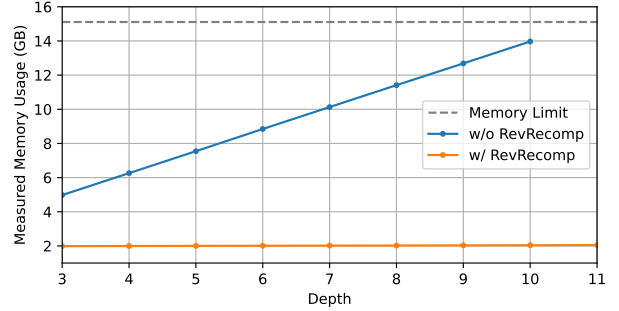


Figure 4. Single GPU memory usage with batch size 64 for training RevBiFPN-S0 on ImageNet with and without reversible recomputation (RevRecomp) as depth is scaled. Reversible recomputation decreases the activation memory complexity from linear to constant. These memory savings can be reallocated to scaling network width and input resolution to produce RevBiFPN S1-S6.

ing network has a parameter and MAC profile similar to common classification networks. RevBiFPN-S0 is then scaled (Appendix C.6) and compared to other network families on the commonly used ImageNet (Deng et al., 2009) benchmark. The heads used and how the network is scaled are described in Appendices C.5 and C.6 respectively. The reference implementation can be found at <https://github.com/CerebrasResearch/RevBiFPN>.

3.1. Memory Savings

The activation memory complexity of training a CV network is $O(nchwd)$ where n is the batch size, c is the number of channels representing the network’s width, h and w specify the input resolution, and d denotes the depth of the network. By decoupling depth from activation memory requirements, reversible networks have an activation memory complexity of $O(nchw)$. Figure 4 shows the measured memory usage of the RevBiFPN-S0 network as the network depth is scaled with and without reversible recomputation. This demonstrates that measured memory usage is approximately constant when reversible recomputation is used but increases linearly otherwise. Appendix C.4 shows how memory scales as the input resolution is scaled.

Table 1. ImageNet accuracy. Extended in Table 11.

MODEL	PARAMS	RES	MACS	TOP1
RevBiFPN-S0	3.42M	224	0.31B	72.8%
RevBiFPN-S1	5.11M	256	0.62B	75.9%
RevBiFPN-S2	10.6M	256	1.37B	79.0%
RevBiFPN-S3	19.6M	288	3.33B	81.1%
RevBiFPN-S4	48.7M	320	10.6B	83.0%
RevBiFPN-S5	82.0M	352	21.8B	83.7%
RevBiFPN-S6	142.3M	352	38.1B	84.2%

Table 2. Training Memory (GB) used per sample.

MODEL	INPUT RESOLUTION		
	TRAIN RES	224	384
RevBiFPN-S6	0.254	0.086	0.291
EFFICIENTNET-B7	5.047	0.673	1.786

4. Experiments

The RevBiFPN family of networks is pretrained on ImageNet and fine-tuned with task-specific heads for detection and segmentation on MS COCO (Lin et al., 2014).

4.1. ImageNet Classification

The experimental setup for ImageNet classification is in Appendix D.1. Although RevBiFPN-S0 and RevBiFPN-S1 can be trained without reversible recomputation, all of the results are shown for networks trained with reversible recomputation. Figure 14 (in Appendix D.3) shows that reversible recomputation does not hurt training. Table 1 summarizes ImageNet classification results. RevBiFPN produces results comparable to classification specific networks. RevBiFPN-S6 uses 38.1B MACs and achieves 84.2% ImageNet Top1 accuracy, making it comparable to EfficientNet-B7 which uses 37B MACs to achieve 84.3% ImageNet Top1 accuracy (Figure 1). Table 2 shows that the GPU memory usage of RevBiFPN-S6 is a fraction of the memory used by EfficientNet-B7 at the training resolution (352 and 600, respectively) as well as frequently used input resolutions of 224 and 384.

4.2. MS COCO

The experimental setup for detection and instance segmentation on MS COCO is in Appendix D.4. Figures 5 and 6 summarize the results in appendix Tables 9 and 10.

Detection Table 9 shows that RevBiFPN-S5 achieves an absolute gain of 3.3% in AP over HRNetV2p-W18 trained using the 2x schedule while uses 0.75GB less memory. RevBiFPN-S3 achieves an absolute gain of 2.5% in AP over HRNetV2p-W18 using fewer MACs and a $\sim 2.4\times$ reduction in training-time memory usage and still outperforms HRNetV2p-W18 by 0.7% AP even if it is trained using a 2x

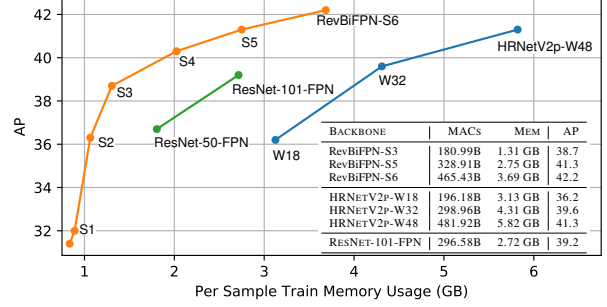


Figure 5. Object detection results on COCO minival in the Faster R-CNN framework using a 1x learning schedule.

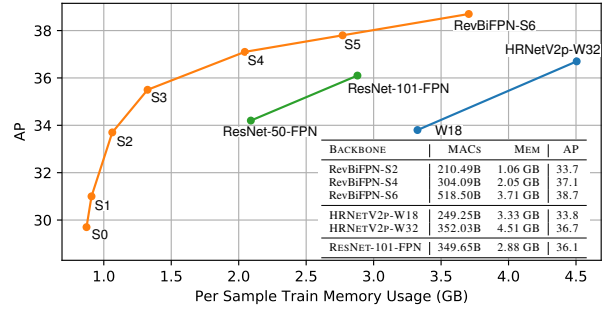


Figure 6. Instance segmentation results on COCO minival in the Mask R-CNN framework using a 1x learning schedule.

schedule. When the scaled HRNetV2p-W48 is trained using a 2x schedule it uses $\sim 1.6\times$ the memory and still does not outperform RevBiFPN-S6 trained using the 1x schedule.

Segmentation The overall performance of RevBiFPN-S2 is comparable to HRNetV2p-W18 but uses $\sim 1.2\times$ fewer MACs and $\sim 2.5\times$ less GPU memory during training. RevBiFPN-S6 outperforms HRNetV2p-W32 by 2% Mask AP and 2.4% Bbox AP while using 1.6GB less memory and still outperforms HRNetV2p-W32 when it is trained using the 2x schedule. Generally, RevBiFPN enables larger inputs for training detection and segmentation systems.

5. Conclusion

Bidirectional multi-scale feature fusion has driven progress in computer vision, but accelerator memory often limits network scale. Reversible methods decrease activation memory complexity but were previously not applicable to bidirectional multi-scale feature fusion. This work introduces the RevSilo, a bidirectional multi-scale feature fusion module that is invertible. The RevSilo is used to design RevBiFPN which is competitive on classification, segmentation, and detection tasks while using a fraction of the memory for training. This makes RevBiFPN applicable to memory-constrained settings such as high-resolution segmentation and detection and enables SOTA research without needing hardware with the latest memory capacity. Future work is in Appendix E.

Acknowledgements

We thank Shreyas Saxena, Nolan Dey, and Valentina Popescu for their help and comments that improved the manuscript. We also thank Ben Wang, Ross Wightman, Lucas Nestler, Jan XMaster, Alexander Mattick, Atli Kosson, Abhinav Venigalla, Xin Wang, Vinay Rao, and Kenyon (Chuan-Yung) Tsai for insightful discussions.

References

- Awiszus, M., Schubert, F., and Rosenhahn, B. TOAD-GAN: Coherent Style Level Generation From a Single Example. In *Proceedings of the AAAI Conference on Artificial Intelligence and Interactive Digital Entertainment*, 2020.
- Bai, S., Kolter, J. Z., and Koltun, V. Deep Equilibrium Models. In Wallach, H., Larochelle, H., Beygelzimer, A., d'Alché-Buc, F., Fox, E., and Garnett, R. (eds.), *Advances in Neural Information Processing Systems*, volume 32. Curran Associates, Inc., 2019.
- Behrmann, J., Grathwohl, W., Chen, R. T., Duvenaud, D., and Jacobsen, J.-H. Invertible Residual Networks. In *International Conference on Machine Learning*, pp. 573–582. PMLR, 2019.
- Bochkovskiy, A., Wang, C.-Y., and Liao, H.-Y. M. YOLOv4: Optimal Speed and Accuracy of Object Detection. *arXiv preprint arXiv:2004.10934*, 2020.
- Brock, A., De, S., Smith, S. L., and Simonyan, K. High-Performance Large-Scale Image Recognition Without Normalization. *arXiv preprint arXiv:2102.06171*, 2021.
- Brügger, R., Baumgartner, C. F., and Konukoglu, E. A Partially Reversible U-Net for Memory-Efficient Volumetric Image Segmentation. In *International Conference on Medical Image Computing and Computer-Assisted Intervention*, pp. 429–437. Springer, 2019.
- Cai, Z. and Vasconcelos, N. Cascade R-CNN: Delving into High Quality Object Detection. In *Proceedings of the IEEE Conference on Computer Vision and Pattern Recognition*, pp. 6154–6162, 2018.
- Chen, C.-C., Yang, C.-L., and Cheng, H.-Y. Efficient and Robust Parallel DNN Training Through Model Parallelism on Multi-GPU Platform. *arXiv preprint arXiv:1809.02839*, 2018a.
- Chen, K., Wang, J., Pang, J., Cao, Y., Xiong, Y., Li, X., Sun, S., Feng, W., Liu, Z., Xu, J., Zhang, Z., Cheng, D., Zhu, C., Cheng, T., Zhao, Q., Li, B., Lu, X., Zhu, R., Wu, Y., Dai, J., Wang, J., Shi, J., Ouyang, W., Loy, C. C., and Lin, D. MMDetection: Open MMLab Detection Toolbox and Benchmark. *arXiv preprint arXiv:1906.07155*, 2019.
- Chen, T., Xu, B., Zhang, C., and Guestrin, C. Training Deep Nets with Sublinear Memory Cost. *arXiv preprint arXiv:1604.06174*, 2016.
- Chen, Y., Wang, Z., Peng, Y., Zhang, Z., Yu, G., and Sun, J. Cascaded Pyramid Network for Multi-Person Pose Estimation. In *Proceedings of the IEEE Conference on Computer Vision and Pattern Recognition*, pp. 7103–7112, 2018b.
- Cheng, B., Xiao, B., Wang, J., Shi, H., Huang, T. S., and Zhang, L. HigherHRNet: Scale-Aware Representation Learning for Bottom-Up Human Pose Estimation. In *Proceedings of the IEEE/CVF Conference on Computer Vision and Pattern Recognition*, pp. 5386–5395, 2020.
- Chiley, V., Sharapov, I., Kosson, A., Koster, U., Reece, R., Samaniego de la Fuente, S., Subbiah, V., and James, M. Online Normalization for Training Neural Networks. In Wallach, H., Larochelle, H., Beygelzimer, A., d'Alché-Buc, F., Fox, E., and Garnett, R. (eds.), *Advances in Neural Information Processing Systems*, volume 32. Curran Associates, Inc., 2019.
- Chun, I. Y., Huang, Z., Lim, H., and Fessler, J. A. Momentum-Net: Fast and Convergent Iterative Neural Network for Inverse Problems. *IEEE Transactions on Pattern Analysis and Machine Intelligence*, 2020.
- Cubuk, E. D., Zoph, B., Shlens, J., and Le, Q. V. RandAugment: Practical Automated Data Augmentation with a Reduced Search Space. In *Proceedings of the IEEE/CVF Conference on Computer Vision and Pattern Recognition Workshops*, pp. 702–703, 2020.
- Dai, Z., Liu, H., Le, Q. V., and Tan, M. CoAtNet: Marrying Convolution and Attention for All Data Sizes. *arXiv preprint arXiv:2106.04803*, 2021.
- Dauvergne, B. and Hascoët, L. The Data-Flow Equations of Checkpointing in Reverse Automatic Differentiation. In *International Conference on Computational Science*, pp. 566–573. Springer, 2006.
- Deng, J., Dong, W., Socher, R., Li, L.-J., Li, K., and Fei-Fei, L. ImageNet: A Large-Scale Hierarchical Image Database. In *2009 IEEE Conference on Computer Vision and Pattern Recognition*, pp. 248–255. IEEE, 2009.
- Dinh, L., Krueger, D., and Bengio, Y. NICE: Non-Linear Independent Components Estimation. In *International Conference on Learning Representations Workshop*, 2014.
- Dinh, L., Sohl-Dickstein, J., and Bengio, S. Density Estimation using Real NVP. In *International Conference on Learning Representations*, 2017.
- Dollár, P., Singh, M., and Girshick, R. Fast and Accurate Model Scaling. In *Proceedings of the IEEE/CVF Con-*

- ference on Computer Vision and Pattern Recognition, pp. 924–932, 2021.
- Dosovitskiy, A., Beyer, L., Kolesnikov, A., Weissenborn, D., Zhai, X., Unterthiner, T., Dehghani, M., Minderer, M., Heigold, G., Gelly, S., Uszkoreit, J., and Houlisby, N. An Image is Worth 16x16 Words: Transformers for Image Recognition at Scale. In *International Conference on Learning Representations*, 2021.
- Fan, H., Xiong, B., Mangalam, K., Li, Y., Yan, Z., Malik, J., and Feichtenhofer, C. Multiscale Vision Transformers. In *Proceedings of the IEEE/CVF International Conference on Computer Vision (ICCV)*, pp. 6824–6835, October 2021.
- Germain, M., Gregor, K., Murray, I., and Larochelle, H. Made: Masked Autoencoder for Distribution Estimation. In *International Conference on Machine Learning*, pp. 881–889. PMLR, 2015.
- Ghiasi, G., Lin, T.-Y., and Le, Q. V. NAS-FPN: Learning Scalable Feature Pyramid Architecture for Object Detection. In *Proceedings of the IEEE/CVF Conference on Computer Vision and Pattern Recognition*, pp. 7036–7045, 2019.
- Girshick, R. Fast R-CNN. In *Proceedings of the IEEE international conference on computer vision*, pp. 1440–1448, 2015.
- Gomez, A. N., Ren, M., Urtasun, R., and Grosse, R. B. The Reversible Residual Network: Backpropagation Without Storing Activations. In *Proceedings of the 31st International Conference on Neural Information Processing Systems*, pp. 2211–2221, 2017.
- Goyal, A., Bochkovskiy, A., Deng, J., and Koltun, V. Non-deep Networks. *arXiv preprint arXiv:2110.07641*, 2021.
- Griewank, A. and Walther, A. Algorithm 799: Revolve: An Implementation of Checkpointing for the Reverse or Adjoint Mode of Computational Differentiation. *ACM Transactions on Mathematical Software (TOMS)*, 26(1): 19–45, 2000.
- He, K., Zhang, X., Ren, S., and Sun, J. Delving Deep into Rectifiers: Surpassing Human-Level Performance on ImageNet Classification. In *Proceedings of the IEEE international conference on computer vision*, pp. 1026–1034, 2015.
- He, K., Zhang, X., Ren, S., and Sun, J. Deep Residual Learning for Image Recognition. In *Proceedings of the IEEE Conference on Computer Vision and Pattern Recognition*, pp. 770–778, 2016.
- He, K., Gkioxari, G., Dollár, P., and Girshick, R. Mask R-CNN. In *Proceedings of the IEEE international conference on computer vision*, pp. 2961–2969, 2017.
- He, K., Girshick, R., and Dollár, P. Rethinking ImageNet Pre-Training. In *Proceedings of the IEEE/CVF International Conference on Computer Vision*, pp. 4918–4927, 2019.
- Hendrycks, D. and Dietterich, T. Benchmarking Neural Network Robustness to Common Corruptions and Perturbations. In *International Conference on Learning Representations*, 2019.
- Howard, A., Sandler, M., Chu, G., Chen, L.-C., Chen, B., Tan, M., Wang, W., Zhu, Y., Pang, R., Vasudevan, V., Le, Q. V., and Adam, H. Searching for MobileNetV3. In *Proceedings of the IEEE/CVF International Conference on Computer Vision*, pp. 1314–1324, 2019.
- Howard, A. G., Zhu, M., Chen, B., Kalenichenko, D., Wang, W., Weyand, T., Andreetto, M., and Adam, H. MobileNets: Efficient Convolutional Neural Networks for Mobile Vision Applications. *arXiv preprint arXiv:1704.04861*, 2017.
- Huang, C.-W., Krueger, D., Lacoste, A., and Courville, A. Neural Autoregressive Flows. In *International Conference on Machine Learning*, pp. 2078–2087. PMLR, 2018a.
- Huang, G., Sun, Y., Liu, Z., Sedra, D., and Weinberger, K. Q. Deep Networks with Stochastic Depth. In *European Conference on Computer Vision*, pp. 646–661. Springer, 2016.
- Huang, G., Chen, D., Li, T., Wu, F., van der Maaten, L., and Weinberger, K. Multi-Scale Dense Networks for Resource Efficient Image Classification. In *International Conference on Learning Representations*, 2018b.
- Huang, Y., Cheng, Y., Bapna, A., Firat, O., Chen, D., Chen, M., Lee, H., Ngiam, J., Le, Q. V., Wu, Y., et al. GPipe: Efficient Training of Giant Neural Networks using Pipeline Parallelism. *Advances in Neural Information Processing Systems*, 32:103–112, 2019.
- Ioffe, S. and Szegedy, C. Batch Normalization: Accelerating Deep Network Training by Reducing Internal Covariate Shift. In *International Conference on Machine Learning*, pp. 448–456. PMLR, 2015.
- Jacobsen, J.-H., Oyallon, E., Mallat, S., and Smeulders, A. W. Multiscale Hierarchical Convolutional Networks. In *International Conference on Machine Learning*. PMLR, 2017.
- Jacobsen, J.-H., Smeulders, A., and Oyallon, E. i-RevNet: Deep Invertible Networks. In *International Conference on Learning Representations*, 2018.

- Ke, T.-W., Maire, M., and Yu, S. X. Multigrid Neural Architectures. In *Proceedings of the IEEE Conference on Computer Vision and Pattern Recognition*, pp. 6665–6673, 2017.
- Keller, T. A., Peters, J. W., Jaini, P., Hoogeboom, E., Forré, P., and Welling, M. Self Normalizing Flows. In *International Conference on Machine Learning*, pp. 5378–5387. PMLR, 2021.
- Kingma, D. P. and Dhariwal, P. Glow: Generative Flow with Invertible 1x1 Convolutions. In Bengio, S., Wallach, H., Larochelle, H., Grauman, K., Cesa-Bianchi, N., and Garnett, R. (eds.), *Advances in Neural Information Processing Systems*, volume 31. Curran Associates, Inc., 2018.
- Kingma, D. P., Salimans, T., Jozefowicz, R., Chen, X., Sutskever, I., and Welling, M. Improved Variational Inference with Inverse Autoregressive FLOW. *Advances in Neural Information Processing Systems*, 29:4743–4751, 2016.
- Kitaev, N., Kaiser, Ł., and Levskaya, A. Reformer: The Efficient Transformer. In *International Conference on Learning Representations*, 2020.
- Kosson, A., Chiley, V., Venigalla, A., Hestness, J., and Koster, U. Pipelined Backpropagation at Scale: Training Large Models without Batches. In Smola, A., Dimakis, A., and Stoica, I. (eds.), *Proceedings of Machine Learning and Systems*, volume 3, pp. 479–501, 2021.
- Krizhevsky, A., Sutskever, I., and Hinton, G. E. ImageNet Classification with Deep Convolutional Neural Networks. *Advances in Neural Information Processing Systems*, 25: 1097–1105, 2012.
- Labatie, A., Masters, D., Eaton-Rosen, Z., and Luschi, C. Proxy-Normalizing Activations to Match Batch Normalization while Removing Batch Dependence. *arXiv preprint arXiv:2106.03743*, 2021.
- LeCun, Y. A., Bottou, L., Bengio, Y., and Haffner, P. Gradient-Based Learning Applied to Document Recognition. *Proceedings of the IEEE*, 86(11):2278–2324, 1998. doi: 10.1109/5.726791.
- Li, Y., Wu, C.-Y., Fan, H., Mangalam, K., Xiong, B., Malik, J., and Feichtenhofer, C. Improved Multiscale Vision Transformers for Classification and Detection. *arXiv preprint arXiv:2112.01526*, 2021.
- Lin, T.-Y., Maire, M., Belongie, S., Hays, J., Perona, P., Ramanan, D., Dollár, P., and Zitnick, C. L. Microsoft COCO: Common Objects in Context. In *European conference on computer vision*, pp. 740–755. Springer, 2014.
- Lin, T.-Y., Dollár, P., Girshick, R., He, K., Hariharan, B., and Belongie, S. Feature Pyramid Networks for Object Detection. In *Proceedings of the IEEE Conference on Computer Vision and Pattern Recognition*, pp. 2117–2125, 2017a.
- Lin, T.-Y., Goyal, P., Girshick, R., He, K., and Dollár, P. Focal Loss for Dense Object Detection. In *Proceedings of the IEEE international conference on computer vision*, pp. 2980–2988, 2017b.
- Liu, S., Qi, L., Qin, H., Shi, J., and Jia, J. Path Aggregation Network for Instance Segmentation. In *Proceedings of the IEEE Conference on Computer Vision and Pattern Recognition*, pp. 8759–8768, 2018.
- Liu, Z., Lin, Y., Cao, Y., Hu, H., Wei, Y., Zhang, Z., Lin, S., and Guo, B. Swin Transformer: Hierarchical Vision Transformer using Shifted Windows. *arXiv preprint arXiv:2103.14030*, 2021.
- Loshchilov, I. and Hutter, F. SGDR: Stochastic Gradient Descent with Warm Restarts. In *International Conference on Learning Representations*, 2017.
- Lu, G., Zhang, W., and Wang, Z. Optimizing Depthwise Separable Convolution Operations on GPUs. *IEEE Transactions on Parallel and Distributed Systems*, 2021.
- MacKay, M., Vicol, P., Ba, J., and Grosse, R. B. Reversible Recurrent Neural Networks. In Bengio, S., Wallach, H., Larochelle, H., Grauman, K., Cesa-Bianchi, N., and Garnett, R. (eds.), *Advances in Neural Information Processing Systems*, volume 31. Curran Associates, Inc., 2018.
- Mehta, S. and Rastegari, M. MobileViT: Light-weight, General-purpose, and Mobile-friendly Vision Transformer. *arXiv preprint arXiv:2110.02178*, 2021.
- Narayanan, D., Harlap, A., Phanishayee, A., Seshadri, V., Devanur, N., Granger, G., Gibbons, P., and Zaharia, M. PipeDream: Generalized Pipeline Parallelism for DNN Training. In *ACM Symposium on Operating Systems Principles (SOSP 2019)*, October 2019.
- Nestler, L. and Gill, D. HomebrewNLP. <https://github.com/HomebrewNLP/HomebrewNLP>, 2021.
- Newell, A., Yang, K., and Deng, J. Stacked Hourglass Networks for Human Pose Estimation. In *European Conference on Computer Vision*, pp. 483–499. Springer, 2016.
- Papamakarios, G., Pavlakou, T., and Murray, I. Masked Autoregressive Flow for Density Estimation. In Guyon, I., Luxburg, U. V., Bengio, S., Wallach, H., Fergus, R., Vishwanathan, S., and Garnett, R. (eds.), *Advances in Neural Information Processing Systems*, volume 30. Curran Associates, Inc., 2017.

- Pendse, M., Thangarasa, V., Chiley, V., Holmdahl, R., Hestness, J., and DeCoste, D. Memory Efficient 3D U-Net with Reversible Mobile Inverted Bottlenecks for Brain Tumor Segmentation. In *BrainLes@MICCAI*, 2020.
- Pétrowski, A., Dreyfus, G., and Girault, C. Performance Analysis of a Pipelined Backpropagation Parallel Algorithm. *IEEE Transactions on Neural Networks*, 4 6:970–81, 1993.
- Qin, Z., Zhang, Z., Li, D., Zhang, Y., and Peng, Y. Diagonalwise Refactorization: An Efficient Training Method for Depthwise Convolutions. In *2018 International Joint Conference on Neural Networks (IJCNN)*, pp. 1–8. IEEE, 2018.
- Radosavovic, I., Kosaraju, R. P., Girshick, R., He, K., and Dollár, P. Designing Network Design Spaces. In *Proceedings of the IEEE/CVF Conference on Computer Vision and Pattern Recognition*, pp. 10428–10436, 2020.
- Rajbhandari, S., Ruwase, O., Rasley, J., Smith, S., and He, Y. ZeRO-Infinity: Breaking the GPU Memory Wall for Extreme Scale Deep Learning. *arXiv preprint arXiv:2104.07857*, 2021.
- Rao, V. and Sohl-Dickstein, J. Is Batch Norm Unique? An Empirical Investigation and Prescription to Emulate the Best Properties of Common Normalizers without Batch Dependence. *arXiv preprint arXiv:2010.10687*, 2020.
- Redmon, J. and Farhadi, A. YOLO9000: Better, Faster, Stronger. In *Proceedings of the IEEE Conference on Computer Vision and Pattern Recognition*, pp. 7263–7271, 2017.
- Redmon, J. and Farhadi, A. YOLOv3: An Incremental Improvement. *arXiv preprint arXiv:1804.02767*, 2018.
- Redmon, J., Divvala, S., Girshick, R., and Farhadi, A. You Only Look Once: Unified, Real-Time Object Detection. In *Proceedings of the IEEE Conference on Computer Vision and Pattern Recognition*, pp. 779–788, 2016.
- Ren, S., He, K., Girshick, R., and Sun, J. Faster R-CNN: Towards Real-Time Object Detection with Region Proposal Networks. In Cortes, C., Lawrence, N., Lee, D., Sugiyama, M., and Garnett, R. (eds.), *Advances in Neural Information Processing Systems*, volume 28, pp. 91–99. Curran Associates, Inc., 2015.
- Ridnik, T., Lawen, H., Noy, A., Baruch, E. B., Sharir, G., and Friedman, I. TRResNet: High Performance GPU-Dedicated Architecture. In *Proceedings of the IEEE/CVF Winter Conference on Applications of Computer Vision*, pp. 1400–1409, 2021.
- Ronneberger, O., Fischer, P., and Brox, T. U-Net: Convolutional Networks for Biomedical Image Segmentation. In *International Conference on Medical image computing and computer-assisted intervention*, pp. 234–241. Springer, 2015.
- Sander, M. E., Ablin, P., Blondel, M., and Peyre, G. Momentum Residual Neural Networks. In *Proceedings of the 38th International Conference on Machine Learning*, pp. 139:9276–9287. PMLR, 2021.
- Sandler, M., Howard, A., Zhu, M., Zhmoginov, A., and Chen, L.-C. MobileNetV2: Inverted Residuals and Linear Bottlenecks. In *Proceedings of the IEEE Conference on Computer Vision and Pattern Recognition*, pp. 4510–4520, 2018.
- Shi, W., Caballero, J., Huszár, F., Totz, J., Aitken, A. P., Bishop, R., Rueckert, D., and Wang, Z. Real-Time Single Image and Video Super-Resolution using an Efficient Sub-Pixel Convolutional Neural Network. In *Proceedings of the IEEE Conference on Computer Vision and Pattern Recognition*, pp. 1874–1883, 2016.
- Simonyan, K. and Zisserman, A. Very Deep Convolutional Networks for Large-Scale Image Recognition. In *International Conference on Learning Representations*, 2015.
- Srivastava, N., Hinton, G., Krizhevsky, A., Sutskever, I., and Salakhutdinov, R. Dropout: A Simple Way to Prevent Neural Networks from Overfitting. *The Journal of Machine Learning Research*, 15(56):1929–1958, 2014.
- Sun, K., Xiao, B., Liu, D., and Wang, J. Deep High-Resolution Representation Learning for Human Pose Estimation. In *Proceedings of the IEEE/CVF Conference on Computer Vision and Pattern Recognition*, pp. 5693–5703, 2019a.
- Sun, K., Zhao, Y., Jiang, B., Cheng, T., Xiao, B., Liu, D., Mu, Y., Wang, X., Liu, W., and Wang, J. High-Resolution Representations for Labeling Pixels and Regions. *arXiv preprint arXiv:1904.04514*, 2019b.
- Szegedy, C., Vanhoucke, V., Ioffe, S., Shlens, J., and Wojna, Z. Rethinking the Inception Architecture for Computer Vision. In *Proceedings of the IEEE conference on computer vision and pattern recognition*, pp. 2818–2826, 2016.
- Tan, M. and Le, Q. EfficientNet: Rethinking Model Scaling for Convolutional Neural Networks. In *International Conference on Machine Learning*, pp. 6105–6114. PMLR, 2019.
- Tan, M. and Le, Q. V. EfficientNetV2: Smaller Models and Faster Training. *arXiv preprint arXiv:2104.00298*, 2021.
- Tan, M., Chen, B., Pang, R., Vasudevan, V., Sandler, M., Howard, A., and Le, Q. V. MnasNet: Platform-Aware Neural Architecture Search for Mobile. In *Proceedings*

- of the *IEEE/CVF Conference on Computer Vision and Pattern Recognition*, pp. 2820–2828, 2019.
- Tan, M., Pang, R., and Le, Q. V. EfficientDet: Scalable and Efficient Object Detection. In *Proceedings of the IEEE/CVF Conference on Computer Vision and Pattern Recognition*, pp. 10781–10790, 2020.
- Tao, A., Sapra, K., and Catanzaro, B. Hierarchical Multi-Scale Attention for Semantic Segmentation. *arXiv preprint arXiv:2005.10821*, 2020.
- Thangarasa, V., Tsai, C.-Y., Taylor, G. W., and Köster, U. Reversible Fixup Networks for Memory-Efficient Training. In *NeurIPS Systems for ML (SysML) Workshop*, 2019.
- Thoma, M. Solving Equations of Lower Unitriangular Matrices. <https://martin-thoma.com/solving-equations-of-unipotent-lower-triangular-matrices/>, 2013.
- Touvron, H., Cord, M., Sablayrolles, A., Synnaeve, G., and Jegou, H. Going Deeper With Image Transformers. In *Proceedings of the IEEE/CVF International Conference on Computer Vision (ICCV)*, pp. 32–42, October 2021.
- Venigalla, A., Kosson, A., Chiley, V., and Köster, U. Adaptive Braking for Mitigating Gradient Delay. In *International Conference on Machine Learning Deep Learning Workshop*, 2020.
- Volin, Y. M. and Ostrovskii, G. M. Automatic Computation of Derivatives With the Use of The Multilevel Differentiating Technique—1. Algorithmic Basis. *Computers & Mathematics with Applications*, 11(11):1099–1114, 1985.
- Wang, J., Sun, K., Cheng, T., Jiang, B., Deng, C., Zhao, Y., Liu, D., Mu, Y., Tan, M., Wang, X., Liu, W., and Xiao, B. Deep High-Resolution Representation Learning for Visual Recognition. *IEEE Transactions on Pattern Analysis and Machine Intelligence*, 2020.
- Wightman, R. PyTorch Image Models. <https://github.com/rwightman/pytorch-image-models>, 2019.
- Wu, Y. and He, K. Group Normalization. In *Proceedings of the European Conference on Computer Vision (ECCV)*, pp. 3–19, 2018.
- Yamazaki, K., Rathour, V. S., and Le, T. Invertible Residual Network with Regularization for Effective Medical Image Segmentation. *arXiv preprint arXiv:2103.09042*, 2021.
- Yang, B., Zhang, J., Li, J., Ré, C., Aberger, C., and De Sa, C. PipeMare: Asynchronous Pipeline Parallel DNN Training. *Proceedings of Machine Learning and Systems*, 3, 2021.
- Yu, F. and Koltun, V. Multi-Scale Context Aggregation by Dilated Convolutions. In *International Conference on Learning Representations*, 2016.
- Yuan, L., Hou, Q., Jiang, Z., Feng, J., and Yan, S. VOLO: Vision Outlooker for Visual Recognition. *arXiv preprint arXiv:2106.13112*, 2021.
- Yun, S., Han, D., Oh, S. J., Chun, S., Choe, J., and Yoo, Y. CutMix: Regularization Strategy to Train Strong Classifiers With Localizable Features. In *Proceedings of the IEEE/CVF International Conference on Computer Vision*, pp. 6023–6032, 2019.
- Zhang, H., Cisse, M., Dauphin, Y. N., and Lopez-Paz, D. mixup: Beyond Empirical Risk Minimization. In *International Conference on Learning Representations*, 2018.
- Zhang, W., Gupta, S., Lian, X., and Liu, J. Staleness-Aware Async-SGD for Distributed Deep Learning. In *Proceedings of the Twenty-Fifth International Joint Conference on Artificial Intelligence, IJCAI’16*, pp. 2350–2356. AAAI Press, 2016. ISBN 9781577357704.
- Zhou, Y., Hu, X., and Zhang, B. Interlinked Convolutional Neural Networks for face parsing. In *International symposium on neural networks*, pp. 222–231. Springer, 2015.
- Zhou, Z., Siddiquee, M. M. R., Tajbakhsh, N., and Liang, J. UNet++: A Nested U-Net Architecture for Medical Image Segmentation. In *Deep Learning in Medical Image analysis and Multimodal Learning for Clinical Decision Support*, pp. 3–11. Springer, 2018.

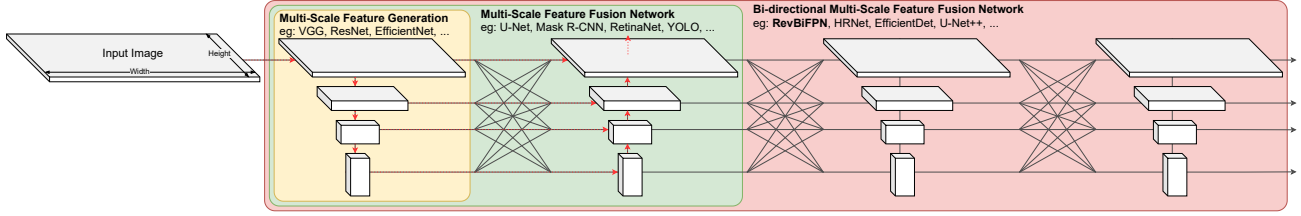


Figure 7. **Connectivity of multi-scale networks:** Features are depicted as boxes and the lines depict the possible connectivity of networks processing features at multiple scales. Networks like VGG (Simonyan & Zisserman, 2015), ResNet (He et al., 2016), and EfficientNet (Tan & Le, 2019) can be used to generate multi-scale features. These features are often fused by networks such as U-Net (Ronneberger et al., 2015), Mask R-CNN (He et al., 2017), or YOLO (Redmon & Farhadi, 2018) for completing spatially sensitive tasks. For example, the multi-scale connectivity of U-Net, with high-resolution outputs, is identified using red arrows. Low-resolution features communicate global information, while high-resolution features are able to capture detailed local information such as texture and object boundaries. By iteratively mixing high and low-resolution features, bidirectional multi-scale feature fusion networks such as HRNet (Sun et al., 2019a), EfficientDet (Tan et al., 2020), and UNet++ (Zhou et al., 2018) promote local and global coherence, boosting performance in CV.

A. Background

Systems using low-resolution features were often applied to image pyramids for detection (Girshick, 2015; Ren et al., 2015; Redmon et al., 2016; Redmon & Farhadi, 2017). Lin et al. (2017a) proposed augmenting a pretrained classification network with a low to high resolution decoder to perform multi-scale feature fusion similar to the U-Net design. Rather than a single high-resolution feature map, the network outputs features from multiple spatial resolutions to create a feature pyramid. The success of the Feature Pyramid Network (FPN) motivated similar methodologies to be used throughout the computer vision community (Redmon & Farhadi, 2018; Bochkovskiy et al., 2020; He et al., 2017; Lin et al., 2017b; Goyal et al., 2021). Bidirectional Feature Pyramid Networks (BiFPNs) further improve performance by iteratively applying multi-scale feature fusion modules (Tan et al., 2020; Ghiasi et al., 2019; Liu et al., 2018; Cai & Vasconcelos, 2018; Chen et al., 2018b). This allows local information from high-resolution feature maps to be repeatedly fused with global input contexts from low-resolution feature maps (Figure 7).

FPNs are often created by using feature fusion modules to augment existing classification networks not originally designed for feature fusion. However, Zhou et al. (2015), Jacobsen et al. (2017), Ke et al. (2017), Huang et al. (2018b), Sun et al. (2019a), Sun et al. (2019b), Wang et al. (2020), Cheng et al. (2020), Fan et al. (2021), and Li et al. (2021) advocate for treating bidirectional multi-scale feature fusion as a first class design principle in computer vision networks and show the effectiveness of this approach for classification, detection, and segmentation. Bidirectional multi-scale feature fusion networks reduce the semantic gap between consecutive feature maps (Zhou et al., 2018). By outputting a feature pyramid, i.e. multi-scale features, these networks allow tasks to be completed at multiple scales. This improves performance, but their memory requirements complicate training and limit scalability.

Achieving SOTA results frequently requires using bidirectional multi-scale feature fusion pyramid networks to processes mega-pixel images. This can results in a single sample’s activations consuming all accelerator memory (Tao et al., 2020). Distributed training setups can accelerate these workloads, but impose other limitations. For instance, needing to use small per accelerator batch sizes precludes the use of Batch Normalization (Ioffe & Szegedy, 2015), requiring alternative normalization methods (Wu & He, 2018; Chiley et al., 2019; Rao & Sohl-Dickstein, 2020; Labatie et al., 2021). Alternatively, researchers can adopt model parallel approaches to scaling models, but this often results in hardware utilization or network optimization issues (Huang et al., 2019; Chen et al., 2018a; Narayanan et al., 2019; Kosson et al., 2021). Another approach to alleviating accelerator memory usage is to offload activations to host (Rajbhandari et al., 2021). However, for bandwidth-constrained systems, this results in poor FLOP utilization. When performing operations with low arithmetic intensity, such as non-linearities or depthwise convolutions (Lu et al., 2021; Qin et al., 2018), on GPUs, limited bandwidth from device memory already results in poor FLOP utilization. Offloading activations to host memory uses bandwidth that is even further constrained, exacerbating the issue.

Volin & Ostrovskii (1985), Griewank & Walther (2000), Dauvergne & Hascoët (2006), and Chen et al. (2016) propose gradient (or reverse) checkpointing where a subset of activations are recomputed instead of being stored. For backpropagation, network activations are needed to compute parameter gradients resulting in an activation memory complexity that is linear with respect to network depth. Checkpointing can reduce this complexity from $O(D)$ to $O(\sqrt{D})$ (Chen et al., 2016).

Reversible models (Gomez et al., 2017; MacKay et al., 2018; Brügger et al., 2019; Pendse et al., 2020; Yamazaki et al., 2021; Sander et al., 2021; Chun et al., 2020; Kitaev et al., 2020; Nestler & Gill, 2021) save memory by recomput-

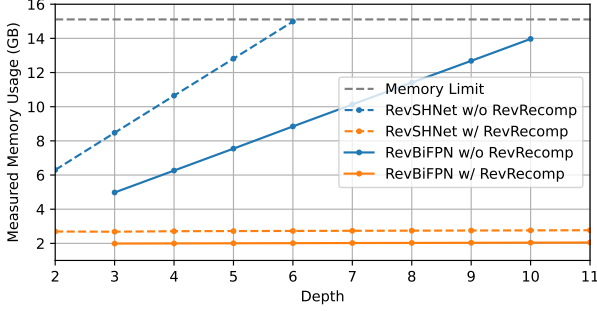


Figure 8. Memory used by RevBiFPN-S0 and a baseline RevSHNet as depth is scaled with and without reversible recomputation (RevRecomp).

ing activations instead of storing them. This decreases the activation memory complexity from linear to constant.³ Reversible recomputation enables SOTA research without needing hardware with the latest memory capacity which prolongs the useful life of existing hardware. As a result, less e-waste is produced, but it comes at the cost of recomputing activations which contributes to the carbon footprint of training reversible models. It should be noted that reversible networks relying only reversible residual block (RevBlock) (Gomez et al., 2017) are not fully reversible. RevBlock cannot operate across different dimensionalities, therefore RevNet (Gomez et al., 2017), and other networks built using RevBlocks, must cache activations in computational blocks that change tensor shape. Fully reversible models have the added benefit of also being used for generation with Normalizing Flow (Dinh et al., 2014; Germain et al., 2015; Dinh et al., 2017; Kingma et al., 2016; Papamakarios et al., 2017; Kingma & Dhariwal, 2018; Huang et al., 2018a; Jacobsen et al., 2018; Keller et al., 2021) but are often not as efficient. For instance, the injective version of i-RevNet (Jacobsen et al., 2018) is a fully reversible variant of RevNet, but requires a 7x increase in size to match RevNet’s performance. Other approaches to reversible recomputation impose architectural limits (Bai et al., 2019), limit optimization (Behrmann et al., 2019; Thangarasa et al., 2019), or are computationally expensive (Behrmann et al., 2019). While any reversible model or method could be used for saving activation memory, none were previously applicable to bidirectional multi-scale feature fusion.

As existing reversible structures keep tensor dimensionality constant, they cannot be directly applied to multi-scale networks such as EfficientDet or HRNet. One approach to produce high-resolution feature maps would be to apply the reversible residual block (Gomez et al., 2017) to an

³When training in layer pipeline mode (Pérowski et al., 1993; Kosson et al., 2021), activation complexity is quadratic with respect to depth. While gradient checkpointing decreases activation memory complexity from $O(D^2)$ to $O(D^{1.5})$ (Yang et al., 2021), reversible recomputation decreases it to $O(D)$.

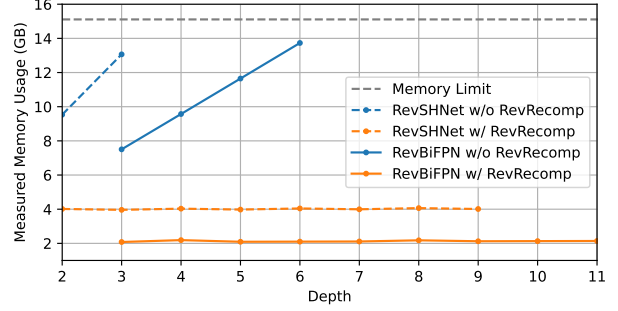


Figure 9. Recreates Figure 8 with an input resolution of 288. This demonstrates how RevBiFPN becomes more favorable as resolution is scaled.

entire subnetwork, such as each hourglass of the Stacked Hourglass Network (Newell et al., 2016). While feasible, the entire subnetwork of activations would still need to be stored, limiting memory savings (Appendix A.1.1). The specific case of the hourglass design also produces high MAC count networks (Appendix A.1.2) and does not provide bidirectional multi-scale feature fusion with a feature pyramid output.

A.1. Reversible Stacked Hourglass Networks

The reversible residual block (Gomez et al., 2017) is only applicable to networks that have constant hidden dimensionality. Stacked Hourglass (Newell et al., 2016) networks are built using a stack of hourglass structures that maintain constant dimensionality. Placing each hourglass structure inside a reversible residual block allows the network to produce high-resolution feature maps without the need to store hidden activations. To enable comparisons with RevBiFPN variants, we implement a Fully Reversible Stacked Hourglass Network, RevSHNet. The baseline RevSHNet uses the MBConv Block, a SpaceToDepth stem, channel counts similar to RevBiFPN-S0 channel counts, and a comparable classification head.

A.1.1. MEMORY

Even with reversible recomputation enabled, RevSHNet needs to store an entire hourglass of activations. With an input size of 224, this results in a memory usage increase of about 40% when compared to the RevBiFPN network (Figure 8). When the input size is increased to 288, RevSHNet uses almost twice the memory used by RevBiFPN (Figure 9). The increased memory usage limits the available memory savings and ultimately limits how much the network can be scaled.

A.1.2. COMPUTE COMPLEXITY

When RevSHNet is scaled, the produced network has a high compute complexity (Figure 10). This is potentially wasteful when scaling to large networks. It should be noted

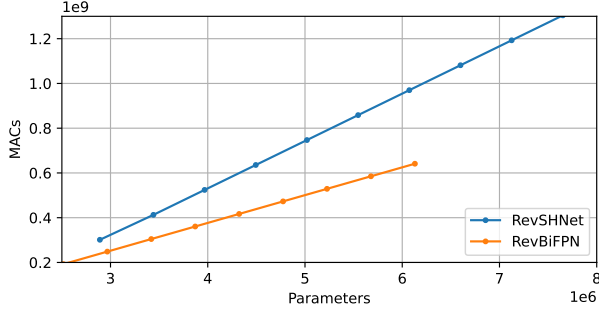


Figure 10. MACs vs Parameter count of RevBiFPN-S0 and a baseline RevSHNet as depth is scaled.

that the above analysis does not take into consideration network performance. Given comparable networks, we expect RevBiFPN to outperform RevSHNet since RevBiFPN has full bidirectional multi-scale feature fusion with a feature pyramid output, whereas RevSHNet does not.

B. RevSilo Equations

The equations for the $N = 4$ RevSilo in Figure 2 are:

$$h_4 = h_0 \quad (1)$$

$$h_5 = g_5(h_1, F_5(h_0)) \quad (2)$$

$$h_6 = g_6(h_2, F_6(h_1, h_0)) \quad (3)$$

$$h_7 = g_7(h_3, F_7(h_2, h_1, h_0)) \quad (4)$$

followed by:

$$h_8 = g_8(h_4, F_8(h_7, h_6, h_5)) \quad (5)$$

$$h_9 = g_9(h_5, F_9(h_7, h_6)) \quad (6)$$

$$h_{10} = g_{10}(h_6, F_{10}(h_7)) \quad (7)$$

$$h_{11} = h_7 \quad (8)$$

The corresponding inverse equations are:

$$h_7 = h_{11} \quad (9)$$

$$h_6 = g_{10}^{-1}(h_{10}, F_{10}(h_7)) \quad (10)$$

$$h_5 = g_9^{-1}(h_9, F_9(h_7, h_6)) \quad (11)$$

$$h_4 = g_8^{-1}(h_8, F_8(h_7, h_6, h_5)) \quad (12)$$

and

$$h_0 = h_4 \quad (13)$$

$$h_1 = g_5^{-1}(h_5, F_5(h_0)) \quad (14)$$

$$h_2 = g_6^{-1}(h_6, F_6(h_1, h_0)) \quad (15)$$

$$h_3 = g_7^{-1}(h_7, F_7(h_2, h_1, h_0)) \quad (16)$$

For the $N = 4$ RevSilo, Equations (1) to (8) are used to compute the forward pass. Instead of saving activations, they can be recomputed during the backward pass using

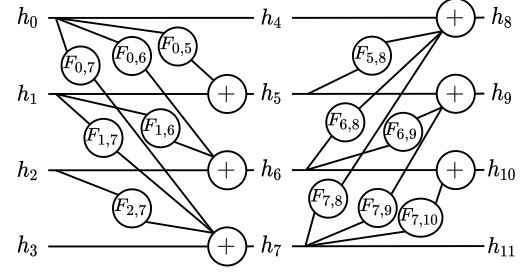


Figure 11. A RevSilo using additive coupling.

Table 3. Down & Up Sampling Operation’s influence on Accuracy.

DOWN / UP SAMPLING	PARAMS	MACS	TOP1
LD / SU	3.49M	75.7M	61.5%
SD / SU	3.28M	67.2M	60.8%
SD / LU	3.47M	69.5M	61.5%

Equations (9) to (16). While the inverse equations must be computed in order, the forward equations allow the N hidden tensors of the RevSilo to be computed simultaneously. This enables more parallelism in the resulting inference network. It should also be noted that if h_i is a scalar, g_i is an addition, and F_i is the dot product operation for all i , then the forward equations can be rewritten as matrix-vector products with unitriangular matrices. The underlying structure that makes unitriangular matrices invertible (Thoma, 2013), makes all coupling structures (Kingma et al., 2016; Germain et al., 2015; Papamakarios et al., 2017; Huang et al., 2018a; Dinh et al., 2014; Gomez et al., 2017) invertible.

B.1. RevSilo with Additive Coupling

While g_i can be any invertible coupling function, this work uses additive coupling as shown in Figure 11.

C. Network Details

As noted in Section 3, RevBiFPN is structurally similar to HRNet. In this section, RevBiFPN is trained on ImageNet for 150 epoch at an input resolution of 96×96 to ablate architectural design decisions.

C.1. Down and Up Sampling Operation

HRNet uses k stride 2 convolution blocks to downsample by 2^k (ld). An alternative downsampling schema would use a single block with stride 2^k and increased kernel size such that the entire input is used to produce the output (sd). To upsample feature maps, HRNet uses a 1×1 convolution paired with an upsample operation in ‘nearest’ mode (su). The 1×1 convolution does not operate in the spatial domain limiting expressivity. To rectify this, the ablations changes the upsampling block to use a 3×3 convolution paired with bilinear upsampling (lu).

Table 4. Stem’s influence on Accuracy.

STEM	PARAMS	MACs	TOP1
CONVOLUTIONAL	3.49M	75.7M	61.5%
SPACEToDEPTH	3.49M	73.7M	61.5%

Table 5. Squeeze-Excite’s influence on Accuracy.

SQUEEZE-EXCITE	PARAMS	MACs	TOP1
NONE	3.40M	75.5M	61.3%
LOW-RES PATH	3.49M	75.7M	61.4%
HIGH-RES PATH	3.46M	76.1M	61.6%

While replacing 1d with sd curbs accuracy on ImageNet, augmenting this change by replacing su with lu results in a total MAC decrease of about 8% while having no affect on ImageNet accuracy (Table 3).

C.2. Backbone Stem

Common practice dictates the use of a convolutional stem for neural network design. Ridnik et al. (2021) propose replacing this with the SpaceToDepth stem. Their work shows this does not effect network accuracy, while increasing the networks GPU throughput performance. Table 4 reaffirms their results and highlights the resulting MAC decrease.

C.3. Squeeze-Excite

Ridnik et al. (2021) note that Squeeze-Excite, when applied to “low-resolution maps, does not get a large accuracy benefit from the global average pooling operation that SE provides.” They advocate for the use of Squeeze-Excite on large as opposed to small spatial resolutions as this provides a good accuracy vs throughput tradeoff. Table 5 affirms their result by showing how Squeeze-Excite when applied to the low-resolution path leaves the network accuracy relatively unaffected, but when applied to the high resolution path, improves network performance.

C.4. Memory as Resolution is Scaled

When scaling width, batch size or input resolution, networks with and without reversible recomputation have the same complexity, but using reversibility creates a memory offset that enables larger variants to be trained. As an example, Figure 12 shows the measured memory usage of RevBiFPN-S0 as the resolution is varied. The reversible variant has an advantageous offset and can run resolutions about 4x larger than is possible with a network without reversible recomputation. On a 16GB system, the largest image a network without reversible recomputation can process is just over 2K×2K. With reversibility, the same network can process images with resolutions up to 8K×8K.

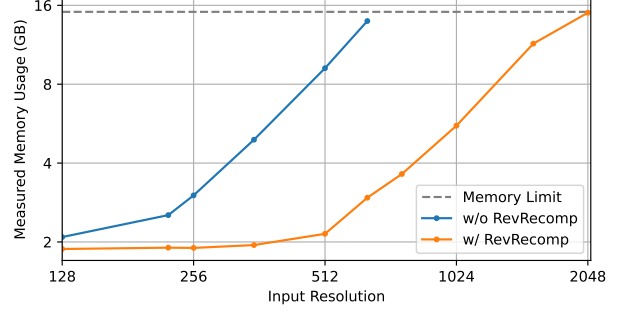


Figure 12. The measured activation memory of training a network using a batch size of 16 on a single GPU with and without reversible recomputation (RevRecomp) as the input resolution is scaled.

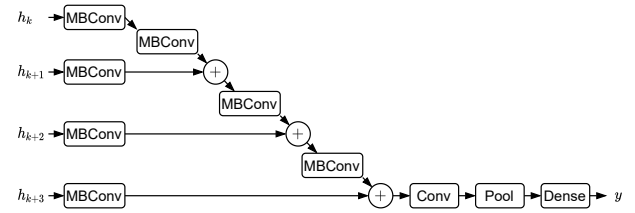


Figure 13. Neck and classification head with feature pyramid input.

C.5. Network Heads

While the RevBiFPN backbone is fully reversible, it can be used with non-reversible heads. Note that before each head is applied, a set of MBConv Blocks is used as a neck, with reverse checkpointing, to transform the output channels of RevBiFPN-S0 to 48, 64, 128, and 320. The dimensionality of the neck and heads are scaled using the width multipliers shown in Table 6. For the detection and segmentation networks, the input resolution is also modified.

ImageNet classification is used to pretrain the RevBiFPN backbone before it is fine-tuned for object detection and segmentation. The backbone outputs a feature pyramid which is transformed using the neck and non-reversible classification head shown in Figure 13. In the head, the highest resolution feature map is downsampled by a factor of 2 using an MBConv Block with stride 2 and is added to the next largest feature map. This is repeated multiple times until all information is aggregated into the lowest resolution feature map. At this point, a 1×1 convolution is applied, followed by global average pooling and a dense layer. This design is inspired by Sun et al. (2019a) but uses the MBConv block.

Object detection and instance segmentation are done with the Faster R-CNN and Mask R-CNN heads provided in MMDetection (Chen et al., 2019).

Table 6. Network width multiplier (m_w), depth (d), and input height and width (h and w) of RevBiFPN variants trained on ImageNet at different scales. Without reversibility, the training setup would need to be modified to accommodate scales past RevBiFPN-S1. Reversible recomputation allows us to train RevBiFPN-S6 with an activation set that is $24\times$ larger than that of RevBiFPN-S1⁴.

MODEL	m_w	d	h AND w
RevBiFPN-S0	1	2	224
RevBiFPN-S1	1.33	2	256
RevBiFPN-S2	2	2	256
RevBiFPN-S3	2.67	3	288
RevBiFPN-S4	4	4	320
RevBiFPN-S5	5.33	4	352
RevBiFPN-S6	6.67	5	352

C.6. Network Scaling

Once the baseline network is designed, scaling the input resolution, network width, and network depth generally results in better performance. Classically, networks such as VGG (Simonyan & Zisserman, 2015) and ResNet (He et al., 2016) focus on scaling network depth. Tan & Le (2019) shows how compound scaling, i.e. scaling all dimensions, results in efficient networks across a range of parameter and MAC counts. Dollár et al. (2021) shows how to scale such that the network run-time is minimized for large networks. Equations (4) and (5) of Dollár et al. (2021) produce a “family of scaling strategies parameterized by α .”

This work uses these scaling strategies but sets $\alpha = 2/3$. While (Dollár et al., 2021) recommends $\alpha = 4/5$, they also show $\alpha = 2/3$ is nearly as fast but enables more depth and resolution scaling. Scaling depth gives added memory benefits in the reversible setting (Section 3.1). Given the outputs of the scaling strategy, m_w is chosen such that channel counts are multiples of 16, the depth is rounded to the nearest integer, and the resolution is set to a multiple of 2^5 (Table 6).

D. Experiments Setup and Hyperparameters

D.1. Classification Setup

The ImageNet dataset is used to pretrain the networks at different scales before they are fine-tuned on downstream tasks. All RevBiFPN variants are pretrained for 350 epochs using 8 GPUs with a per GPU batch size of 64. SGD is used with a learning rate of 0.1 and momentum of 0.9, and an exponential moving average (EMA) of the network parameters is used with a decay of 0.9999. A 5 epoch learning rate warm-up is used with a starting learning rate of 10^{-3} followed by cosine decay (Loshchilov & Hutter, 2017). The

⁴Without reversible recomputation, the memory used for activations, $n \times c \times h \times w \times d$, dominates accelerator memory usage. $|\text{RevBiFPN-S6}| / |\text{RevBiFPN-S1}| = (n \times 6.67c \times 352 \times 352 \times 5) / (n \times 1.33c \times 256 \times 256 \times 2) = 23.7$.

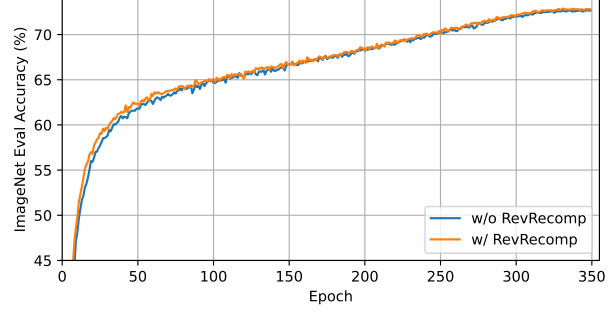


Figure 14. ImageNet validation accuracy when training RevBiFPN-S0 with and without reversible recomputation (RevRecomp).

last 10 epochs use a constant learning rate of 10^{-4} . The network uses batch normalization with a momentum of 0.9 and epsilon of 10^{-3} . The running means and standard deviations are averaged across all accelerators at the end of each epoch. Training is regularized using label smoothing (Szegedy et al., 2016), weight decay, dropout (Srivastava et al., 2014), stochastic depth (Huang et al., 2016), CutMix (Yun et al., 2019), mixup (Zhang et al., 2018), and RandAugment (Cubuk et al., 2020). Details can be found in Appendix D.2. Tuning the hyperparameters above could result in further improvement.

D.2. ImageNet Training and Regularization

Training is regularized using label smoothing (Szegedy et al., 2016), weight decay, dropout (Srivastava et al., 2014), stochastic depth (Huang et al., 2016), CutMix (Yun et al., 2019), mixup (Zhang et al., 2018), and the timm library (Wightman, 2019) variant of RandAugment (Cubuk et al., 2020). To prevent larger scales of the network from overfitting, regularization increases with network scale. Without knowing how much augmentation was needed for each network, training began with the regularization shown in Table 8.

When the validation accuracy of the EMA model began to plateau, the regularization of the models was increased. The final regularization used for each network is shown in Table 7.

D.3. Training With and Without Reversibility

Under infinite precision, training with and without reversible recomputation would produce identical results. Figure 14 shows that while there are differences using finite precision, these are inconsequential. Training RevBiFPN-S0 with reversible recomputation requires only 2GB of accelerator memory and produces results that are nearly indistinguishable from regular training which consumes 12GB of accelerator memory.

Table 7. Weight decay (WD), dropout, number of RandAugment ops applied (N), mixup, CutMix, and stochastic depth used at the end of training. Label smoothing uses a coefficient of 0.1 and RandAugment uses a magnitude of 9 and mstd of 0.5.

MODEL	WD	DROPOUT	N	MIXUP	CUTMIX	STOCHASTIC DEPTH
RevBiFPN-S0	4×10^{-5}	0.25	2	0.00	0.0	0.00
RevBiFPN-S1	4×10^{-5}	0.25	2	0.00	0.0	0.00
RevBiFPN-S2	4×10^{-5}	0.3	3	0.00	0.0	0.00
RevBiFPN-S3	4×10^{-5}	0.3	3	0.10	1.0	0.05
RevBiFPN-S4	2×10^{-5}	0.4	4	0.10	1.0	0.10
RevBiFPN-S5	2×10^{-5}	0.4	4	0.20	1.0	0.10
RevBiFPN-S6	2×10^{-5}	0.6	5	0.20	1.0	0.30

Table 8. Initial dropout, number of RandAugment ops applied (N). Training initially uses a weight decay of 4×10^{-5} , label smoothing coefficient of 0.1, the RandAugment magnitude is set to 9, and mstd is set to 0.5, and the network is trained without mixup, CutMix, or stochastic depth.

MODEL	DROPOUT	N
RevBiFPN-S0	0.25	2
RevBiFPN-S1	0.25	2
RevBiFPN-S2	0.25	2
RevBiFPN-S3	0.25	2
RevBiFPN-S4	0.4	4
RevBiFPN-S5	0.4	4
RevBiFPN-S6	0.5	5

D.4. MS COCO Experiments Setup

Experimental results are presented on the MS COCO 2017 detection dataset, which contains about 118k images for training, 5k for validation (`minival`) and ~ 20 k testing without provided annotations (`test-dev`). The average precision (AP) metric is adopted, which is the standard COCO evaluation procedure. The multi-level feature representations from RevBiFPN, as shown in Figure 3, are applied for the task of object detection and instance segmentation. There is no additional data augmentation besides the standard horizontal flipping. For training and testing, the input images are resized such that the shorter edge is 800 pixels (Lin et al., 2017a). Evaluation is performed using a single image scale.

RevBiFPN is compared with HRNet and ResNet. The object detection performance is evaluated on COCO `minival` under the two-stage anchor-based framework, Faster R-CNN (Ren et al., 2015). Faster R-CNN models are trained using RevBiFPN, HRNet, and ResNet pretrained backbones on the MMDetection open-source object detection toolbox (Chen et al., 2019). Table 9 summarizes parameters, the evaluation MACs per sample,⁵ the GPU memory usage during training, and scores. Similar to (Sun et al., 2019a), the GPU memory usage is measured during training on a 4 GPU system, with an input size of 800×1333 and batch size of 8.

The Mask R-CNN (He et al., 2017) framework is used to evaluate RevBiFPN for object detection and instance segmentation on MS COCO. The results are obtained on the MMDetection toolbox and are summarized in Table 10.⁵

Baseline results are from Wang et al. (2020). RevBiFPN is pretrained for 350 epochs whereas Wang et al. (2020) pretrains for 100 epochs. He et al. (2019) shows how longer fine-tuning schedules can entirely eliminate the benefits of pretraining. This can make a network trained for 100 epochs and fine-tuned with a 2x schedule comparable to a network trained for 350 epochs and fine-tuned with a 1x schedule. Tables 9 and 10 include results from 1x and 2x schedules to enable such comparisons. Tan et al. (2020) fine-tunes networks for up to 600 epochs. As a result, EfficientDet (Tan et al., 2020) serves as a strong baseline for work pursuing SOTA results. Being subject to resource constraints, we do not make such comparisons and instead focus on the memory saving, but note that Tan et al. (2020) shows how longer training schedules even further differentiate networks using bidirectional multi-scale feature fusion.

Tables 9 and 10 extend the results in Figures 5 and 6

E. Future Work

Reversible networks recompute activations during the backward pass instead of storing the activations computed in the forward pass. The reconstruction error of recomputation, the impact of numerical precision on this error, and the effect this has on optimization are all potential research directions. Along with RevBiFPN’s sensitivity to numerical precision, research could also look at RevBiFPN’s sensitivity to normalizers, network sparsification methods, adversarial perturbations, and delayed gradient optimization along with its mitigation methods (Zhang et al., 2016; Venigalla et al., 2020). Additionally, RevBiFPN generates entire feature pyramids at multiple semantic levels making it amenable to

⁵The tool used to analyze the evaluation MACs per sample for the various models can be found here: https://github.com/open-mmlab/mmcv/blob/master/mmcv/cnn/utils/flops_counter.py

Table 9. Object detection results on COCO minival in the Faster R-CNN framework. LS = learning schedule. 1x = 12 epochs, 2x = 24 epochs. Mem = per sample GPU memory used during training.

BACKBONE	PARAMS	MACS	MEM	LS	AP	AP ₅₀	AP ₇₅	AP _S	AP _M	AP _L
RevBiFPN-S0	19.55M	135.12B	0.84GB	1x	31.4	51.5	33.3	17.8	34.3	40.9
RevBiFPN-S1	20.48M	140.66B	0.89GB	1x	32.0	52.0	34.1	18.3	35.7	43.0
RevBiFPN-S2	23.86M	157.42B	1.07GB	1x	36.3	57.4	39.3	20.8	39.6	46.6
RevBiFPN-S3	30.40M	180.99B	1.31GB	1x	38.7	60.0	41.4	23.1	42.0	50.4
RevBiFPN-S4	52.88M	251.02B	2.03GB	1x	40.3	60.5	44.0	23.7	44.3	52.4
RevBiFPN-S5	77.83M	328.91B	2.75GB	1x	41.3	62.7	44.8	24.8	45.6	52.5
RevBiFPN-S6	127.51M	465.43B	3.69GB	1x	42.2	63.5	45.8	25.7	46.5	54.0
HRNetV2P-W18	27.48M	196.18B	3.13GB	1x	36.2	57.3	39.3	20.7	39.0	46.8
HRNetV2P-W18	27.48M	196.18B	3.13GB	2x	38.0	58.9	41.5	22.6	40.8	49.6
HRNetV2P-W32	47.28M	298.96B	4.31GB	1x	39.6	61.0	43.3	23.7	42.5	50.5
HRNetV2P-W32	47.28M	298.96B	4.31GB	2x	40.9	61.8	44.8	24.4	43.7	53.3
HRNetV2P-W48	83.36M	481.92B	5.82GB	1x	41.3	62.8	45.1	25.1	44.5	52.9
HRNetV2P-W48	83.36M	481.92B	5.82GB	2x	41.8	62.8	45.9	25.0	44.7	54.6
RESNET-50-FPN	41.53M	216.70B	1.81GB	1x	36.7	58.3	39.9	20.9	39.8	47.9
RESNET-50-FPN	41.53M	216.70B	1.81GB	2x	37.6	58.7	41.3	21.4	40.8	49.7
RESNET-101-FPN	60.52M	296.58B	2.72GB	1x	39.2	61.1	43.0	22.3	42.9	50.9
RESNET-101-FPN	60.52M	296.58B	2.72GB	2x	39.8	61.4	43.4	22.9	43.6	52.4

 Table 10. Instance segmentation and object detection results on COCO minival in the Mask R-CNN framework.

BACKBONE	PARAMS	MACS	MEM	LS	MASK				BBOX			
					AP	AP _S	AP _M	AP _L	AP	AP _S	AP _M	AP _L
RevBiFPN-S0	22.19M	188.20B	0.87GB	1x	29.7	13.5	32.3	44.2	31.4	17.8	34.3	40.9
RevBiFPN-S1	23.12M	193.73B	0.91GB	1x	31.0	14.1	33.3	45.3	34.0	19.0	37.0	44.6
RevBiFPN-S2	26.50M	210.49B	1.06GB	1x	33.7	16.0	35.9	49.2	37.1	21.7	40.2	48.5
RevBiFPN-S3	33.04M	232.92B	1.32GB	1x	35.5	17.4	38.4	50.9	39.4	23.6	43.1	50.9
RevBiFPN-S4	55.50M	304.09B	2.05GB	1x	37.1	17.8	40.1	53.4	41.5	24.2	45.4	53.9
RevBiFPN-S5	80.47M	381.99B	2.77GB	1x	37.8	18.5	40.7	54.3	42.2	25.5	46.3	54.3
RevBiFPN-S6	130.15M	518.50B	3.71GB	1x	38.7	19.8	41.7	55.2	43.3	26.9	47.4	55.6
HRNetV2P-W18	30.13M	249.25B	3.33GB	1x	33.8	15.6	35.6	49.8	37.1	21.9	39.5	47.9
HRNetV2P-W18	30.13M	249.25B	3.33GB	2x	35.3	16.9	37.5	51.8	39.2	23.7	41.7	51.0
HRNetV2P-W32	49.92M	352.03B	4.51GB	1x	36.7	17.3	39.0	53.0	40.9	24.5	43.9	52.2
HRNetV2P-W32	49.92M	352.03B	4.51GB	2x	37.6	17.8	40.0	55.0	42.3	25.0	45.4	54.9
RESNET-50-FPN	44.17M	269.78B	2.09GB	1x	34.2	15.7	36.8	50.2	37.8	22.1	40.9	49.3
RESNET-50-FPN	44.17M	269.78B	2.09GB	2x	35.0	16.0	37.5	52.0	38.6	21.7	41.6	50.9
RESNET-101-FPN	63.16M	349.65B	2.88GB	1x	36.1	16.2	39.0	53.0	40.0	22.6	43.4	52.3
RESNET-101-FPN	63.16M	349.65B	2.88GB	2x	36.7	17.0	39.5	54.8	41.0	23.4	44.4	53.9

deep supervision which could aid optimization to improve performance (Newell et al., 2016; Zhou et al., 2018).

Tuning a model for inference is an important aspect of a models development and it would be prudent to make device specific optimizations before deploying RevBiFPN to a specific inference platform since GPU speeds does not correlate with speeds on inference devices (Mehta & Rastegari, 2021). Using the MBConv building block produces networks which are generally fast on mobile inference platforms (Howard et al., 2017; Sandler et al., 2018), but exploring the use of ResNet, ResNeXt, or Transformer blocks could produce networks better optimized for other metrics. The building block could also use 3D convolutions for application to highly memory-intensive 3D workloads. Future work could also explore other architectural modifications such as the use of dilated convolutions (Yu & Koltun, 2016) or weight sharing for repeated blocks in RevBiFPN to produce more parameter efficient networks. With regards to scaling, future work could investigate alternate strategies and the effects of modifying N , the number of spatial resolutions in the feature pyramid. In general, the architectural design could be improved by Neural Architecture Search (Tan et al., 2019; Ghiasi et al., 2019; Tan & Le, 2019).

Lastly, the RevSilo and RevBiFPN could be applied to other domains. The RevSilo can be used as a reversible multi-modal fusion module or for fusing information from multiple input sensors. For instance, self-driving cars use multiple imaging systems. Training these systems can be highly memory-intensive, but using RevSilo to fuse different inputs could provide a memory-efficient solution. Lastly, given RevBiFPN is fully reversible, it can be used for flow-based generation. Awiszus et al. (2020) argue that multi-scale processing is needed in GAN generation as it provides local and global coherence. Prior to this work, bidirectional multi-scale feature fusion wasn't possible in flow models, but now the RevSilo and RevBiFPN can provide local and global coherence for flow-based generation.

F. ImageNet Model Comparisons

Table 11 extends Table 1. This enable comparisons of RevBiFPN variants to other state of the art networks trained on ImageNet1k.

Table 11. Models trained using only ImageNet1k. While most networks are trained using 300 to 400 epochs, HRNet and RegNetY use a 100 epoch training schedule.

MODEL	PARAMS	TRAIN RES	RES	MACS	TOP1
RevBiFPN-S0	3.42M	224	224	0.31B	72.8%
RevBiFPN-S1	5.11M	256	256	0.62B	75.9%
RevBiFPN-S2	10.6M	256	256	1.37B	79.0%
RevBiFPN-S3	19.6M	288	288	3.33B	81.1%
RevBiFPN-S4	48.7M	320	320	10.6B	83.0%
RevBiFPN-S5	82.0M	352	352	21.8B	83.7%
RevBiFPN-S6	142.3M	352	352	38.1B	84.2%
EFFICIENTNET-B0	5.3M	224	224	0.39B	77.1%
EFFICIENTNET-B1	7.8M	240	240	0.70B	79.1%
EFFICIENTNET-B2	9.2M	260	260	1.0B	80.1%
EFFICIENTNET-B3	12M	300	300	1.8B	81.6%
EFFICIENTNET-B4	19M	380	380	4.2B	82.9%
EFFICIENTNET-B5	30M	456	456	9.9B	83.6%
EFFICIENTNET-B6	43M	528	528	19B	84.0%
EFFICIENTNET-B7	66M	600	600	37B	84.3%
EFFICIENTNET-B5	30M	456	456	9.9B	83.9%
EFFICIENTNET-B7	66M	600	600	37B	85.0%
EFFICIENTNETV2-S	24M	128 - 300	300	8.8B	83.9%
EFFICIENTNETV2-M	55M	128 - 380	380	24B	85.1%
EFFICIENTNETV2-L	121M	128 - 380	380	53B	85.7%
NFNET-F0	72.0M	192	256	12B	83.6%
NFNET-F1	133M	224	320	36B	84.7%
NFNET-F2	194M	256	352	63B	85.1%
NFNET-F3	255M	320	416	115B	85.7%
NFNET-F4	316M	384	512	215B	85.9%
NFNET-F5	377M	416	544	290B	86.0%
VOLO-D1	27M	224	384	22.8B	85.2%
VOLO-D2	59M	224	384	46.1B	86.0%
VOLO-D3	86M	224	448	67.9B	86.3%
VOLO-D4	193M	224	448	197B	86.8%
VOLO-D5	269M	224	448	304B	87.0%
VOLO-D5	269M	224	512	412B	87.1%
ViT-B/16	86.0M	384	384	55.4B	77.91%
ViT-L/16	307M	384	384	191B	76.53%
SWIN-T	29M	224	224	4.5B	81.3%
SWIN-S	50M	224	224	8.7B	83.0%
SWIN-B	88M	224	384	47.0B	84.5%
CoATNet-0	25M	224	384	13.4B	83.9%
CoATNet-1	42M	224	384	27.4B	85.1%
CoATNet-2	75M	224	384	49.8B	85.7%
CoATNet-2	75M	224	512	96.7B	85.9%
CoATNet-3	168M	224	384	107B	85.8%
CoATNet-3	168M	224	512	203B	86.0%
CAiT-XXS-24	12.0M	224	384	9.5B	80.4%
CAiT-XXS-36	17.3M	224	384	14.2B	81.8%
CAiT-XS-24	26.6M	224	384	19.3B	83.8%
CAiT-XS-36	38.6M	224	384	28.8B	84.3%
CAiT-S-24	46.9M	224	384	32.2B	84.3%
CAiT-S-36	68.2M	224	384	48.0B	85.0%
CAiT-S-48	89.5M	224	384	63.8B	85.1%
CAiT-M-24	185.9M	224	384	116.1B	84.5%
CAiT-M-36	270.9M	224	384	173.3B	84.9%
HRNET-W18-C	21.3M	224	224	3.99B	76.8%
HRNET-W30-C	37.7M	224	224	7.55B	78.2%
HRNET-W32-C	41.2M	224	224	8.31B	78.5%
HRNET-W40-C	57.6M	224	224	11.8B	78.9%
HRNET-W44-C	67.1M	224	224	13.9B	78.9%
HRNET-W48-C	77.5M	224	224	16.1B	79.3%
HRNET-W64-C	128M	224	224	26.9B	79.5%
REGNETY-200MF	3.2M	224	224	0.2B	70.4%
REGNETY-400MF	4.3M	224	224	0.4B	74.1%
REGNETY-600MF	6.1M	224	224	0.6B	75.5%
REGNETY-800MF	6.3M	224	224	0.8B	76.3%
REGNETY-1.6GF	11.2M	224	224	1.6B	78.0%
REGNETY-3.2GF	19.4M	224	224	3.2B	79.0%
REGNETY-4.0GF	20.6M	224	224	4.0B	79.4%
REGNETY-6.4GF	30.6M	224	224	6.4B	79.9%
REGNETY-8.0GF	39.2M	224	224	8.0B	79.9%
REGNETY-12GF	51.8M	224	224	12.1B	80.3%
REGNETY-16GF	83.6M	224	224	15.9B	80.4%
REGNETY-32GF	145.0M	224	224	32.3B	81.0%